

Optical Rashba Effect in a Light-Emitting Perovskite Metasurface

Jingyi Tian, Giorgio Adamo,* Hailong Liu, Maciej Klein, Song Han, Hong Liu, and Cesare Soci*

The Rashba effect, i.e., the splitting of electronic spin-polarized bands in the momentum space of a crystal with broken inversion symmetry, has enabled the realization of spin-orbitronic devices, in which spins are manipulated by spin-orbit coupling. In optics, where the helicity of light polarization represents the spin degree of freedom for spin-momentum coupling, the optical Rashba effect is manifested by the splitting of optical states with opposite chirality in the momentum space. Previous realizations of the optical Rashba effect relied on passive devices determining the surface plasmon or light propagation inside nanostructures, or the directional emission of chiral luminescence when hybridized with light-emitting media. An active device underpinned by the optical Rashba effect is demonstrated here, in which a monolithic halide perovskite metasurface emits highly directional chiral photoluminescence. An all-dielectric metasurface design with broken in-plane inversion symmetry is directly embossed into the high-refractive-index, light-emitting perovskite film, yielding a degree of circular polarization of photoluminescence of 60% at room temperature.

(spatial) distributions, thus offering a powerful tool to manipulate incoherent light emission.^[1–5]

Metasurface design dictates the nature of the VOS. For example, if the structure has in-plane inversion symmetry (e.g., square lattices of circular holes, pillars or gratings), some of the VOS with frequency overlapping with the continuum cannot radiate in free space due to the symmetry mismatch with plane waves, thereby remaining perfectly confined within the structure.^[6] Such VOS are referred to as symmetry-protected bound states in the continuum (BICs). Due to their highly confined nature, BICs display extremely high radiative quality factors (theoretically infinite) and manifest themselves as far-field intensity and polarization singularities of integer topological charges in the luminescence emitted by the metasurface.^[7–10] Conversely, if the in-plane

inversion symmetry of the structure is broken (e.g., square lattices of triangular metamolecules), the integer charges of the BICs decompose into pairs of half-integer charges associated with circularly polarized states in the momentum space.^[11,12] By designing the metasurface in such a way that the wavelengths of its VOS overlap with the luminescence spectrum of the light-emitting medium, emission is funneled into the radiative channels opened by the VOS, whose polarization and directivity can be freely and precisely engineered. This effectively realizes the optical analog of the Rashba effect in condensed matter.^[1,3–5,13–19]

After the theoretical prediction of its occurrence in zinc blende and wurtzite crystal lattices,^[20,21] the Rashba effect has been observed in a variety of condensed-matter systems, including 2D semiconductors, surfaces of metals, heterostructures and topological insulators.^[22,23] Recently, the discovery of the Rashba effect in halide perovskites has triggered an enormous interest for their potential application in spintronics.^[24–27] Besides their unique electronic and spintronic properties, halide perovskites are an emerging optical platform for all-dielectric metamaterials that combine light confinement at the nanoscale and strong light-matter interaction^[28] with excellent radiative properties.^[29,30] This owes to the rare combination of compositionally tunable spectrum, high luminescence yield, and high refractive index ($n > 2$). To the best of our knowledge, materials with comparable properties are limited to III–V compound semiconductors, such as GaAs, which are much more


1. Introduction

Luminescence from light-emitting media is generally omnidirectional, unpolarized, incoherent and oftentimes weak. This is unsuitable for applications that require high brightness, directionality, and polarization control. Metasurfaces consisting of a periodic arrangement of artificial atoms can create delocalized virtual optical states (VOS) with enhanced local density of states and deterministic energy (spectral) and momentum

J. Tian, G. Adamo, M. Klein, S. Han, C. Soci
Centre for Disruptive Photonic Technologies
TPI
Nanyang Technological University
21 Nanyang Link, Singapore 637371, Singapore
E-mail: g.adamo@ntu.edu.sg; csoci@ntu.edu.sg

J. Tian, G. Adamo, M. Klein, S. Han, C. Soci
Division of Physics and Applied Physics
School of Physical and Mathematical Sciences
Nanyang Technological University
21 Nanyang Link, Singapore 637371, Singapore

H. Liu, H. Liu
Institute of Materials Research and Engineering
Agency for Science, Technology and Research (A*STAR)
2 Fusionopolis Way, Singapore 138634, Singapore

 The ORCID identification number(s) for the author(s) of this article can be found under <https://doi.org/10.1002/adma.202109157>.

DOI: 10.1002/adma.202109157

costly and difficult to grow/pattern than solution-processed perovskite films. Direct embossing by nanoimprint lithography is also available for large-area patterning of perovskite films. Early realizations of dielectric perovskite metamaterials have been primarily focused on the demonstration of luminescence enhancement,^[31,32] with a few works recently extending the concept to the control of polarization and spatial distribution of microlaser emission.^[8–10] A hallmark of polarization control, emission of circularly polarized light of chosen helicity, has only been demonstrated by incorporating chiral ligands into the inorganic framework of the perovskites, yet with a degree of circular polarization (DOP) barely exceeding $\pm 10\%$ at room temperature,^[18,19,33] which is impractically small for chiral emitting device applications. Here we exploit the combination of metamaterial design strategies with the unique optoelectronic properties of halide perovskites as a new avenue for the implementation of highly chiral emission sources underpinned by the optical Rashba effect and demonstrate a monolithic, all-dielectric light-emitting metasurface with enhanced and directional chiral photoluminescence with a $\pm 60\%$ degree of circular polarization at room temperature—a sixfold increase compared to state of the art chiral perovskites.^[18,19,33]

2. Results and Discussion

For this proof of principle demonstration, we spin-cast a 170 nm-thick film of methylammonium lead-iodide (MAPbI₃) perovskite (optical properties in Supporting Information, section I) in which polycrystalline domains are randomly distributed. This results in uniformly distributed and unpolarized radiation, resembling isotropic media made of an ensemble of randomly oriented dipoles with unrelated initial phases and locations (Figure 1a-i), which can be treated as a superposition of chiral emitters with opposite chirality. The metasurface consists of a periodic array of triangular metamolecules—a broken in-plane inversion symmetry design which results in splitting of integer charges of BICs ($|1\rangle$) and gives rise to a pair of purely circularly polarized VOS ($|\pm\frac{1}{2}\rangle$), details in Supporting

Information, section II) in the momentum space located above the light cone and below the diffraction limit with nonzero intensity and opposite handedness (Figure 1a-ii). The VOS offer enhanced radiation channels into the far field with well-defined distributions of polarization and in-plane wave vectors (Figure 1b). Such metasurface was realized by nanoimprint lithography (Figure 1c).

The VOS of the metasurface can be identified by its optical band diagram. The calculated transverse electric (TE) polarized optical bands along the x -axis are illustrated in Figure 2a, where the wavevectors are linked to the far-field radiation angle θ of the VOS in the x - z plane, by the relation $k_x/k_0 = \sin\theta$. The TE2 band, highlighted in green, which manifests as a quadrupole state at $k = 0$, shows low dispersion within the emission spectral range of MAPbI₃ around $\lambda = 800$ nm. The z component of the magnetic field, H_z , shows an asymmetric distribution of the TE2 mode in the x - y plane (inset in Figure 2a), dictated by the broken in-plane inversion symmetry of the design. When TE2 is projected into the far-field as polarization vectors, $E_{xy}(\theta) = (E_x(\theta), E_y(\theta))$, it is possible to calculate the polarization handedness of the electric field intensity as a function of the radiation angle. The resulting angular distribution of circularly polarized intensities with opposite handedness, $I_R(\theta)$ and $I_L(\theta)$, is strongly directional into different sectors of the far field ($\pm\theta$), as shown in Figure 2b. The DOP of the radiated field (Figure 2c) expressed as $\text{DOP}(\theta) = [I_R(\theta) - I_L(\theta)]/[I_R(\theta) + I_L(\theta)]$, reveals a quite rich far-field polarization distribution associated with the TE2 band (the degree of polarization of the VOS associated with the TE2 band is reflected in the band diagram in Figure S2, Supporting Information). At $\theta = 0$ (normal direction), the mode polarization is linear along the x axis, here denoted by H . Moving just off normal in opposite directions along the x -axis, a pair of purely circularly polarized VOS of opposite handedness ($\text{DOP} = \pm 100\%$), denoted as $\text{RC}(|+\frac{1}{2}\rangle)$ and $\text{LC}(|-\frac{1}{2}\rangle)$, is generated. Going further off the normal, the two circular polarizations first evolve into linear polarization along the y axis, denoted by V , before switching handedness and reaching a $\text{DOP}_{\text{sim}} > \mp 60\%$. The evolution of the DOP can be mapped onto a Poincaré sphere (inset of Figure 2c) where it traces

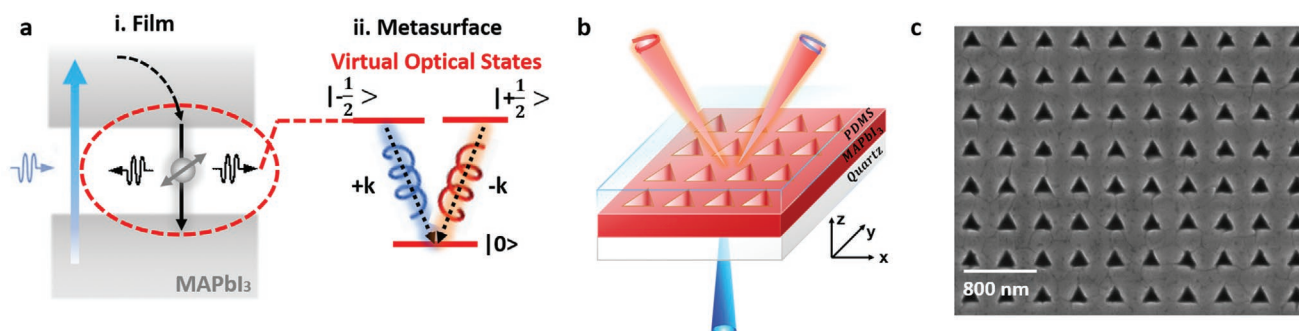


Figure 1. Perovskite metasurfaces for directional control of chiral luminescence. a) Diagram of photoluminescence (PL) from MAPbI₃. i) PL from a MAPbI₃ film due to near-band-edge transition resembles the emission from multiple dipoles, which is isotropic and unpolarized. ii) PL from a MAPbI₃ metasurface with well-controlled far-field polarization distributions due to the splitting of virtual optical states (VOS) with opposite chirality ($|\pm\frac{1}{2}\rangle$) in momentum space. b) Schematic of optical Rashba effect in an all-dielectric in-plane inversion-symmetry-broken perovskite metasurface patterned with a square lattice of equilaterally triangular holes and sandwiched between a quartz ($n = 1.5$) substrate and a PDMS ($n = 1.5$) layer. The side length of the hole is 220 nm and the period is 400 nm. The metasurface is excited by a blue laser (405 nm) from the back side and the PL with opposite chirality is routed into opposite sectors of the hemisphere. c) Scanning electron microscopy image of a MAPbI₃ metasurface made by nanoimprinting lithography. The scale bar is 800 nm.

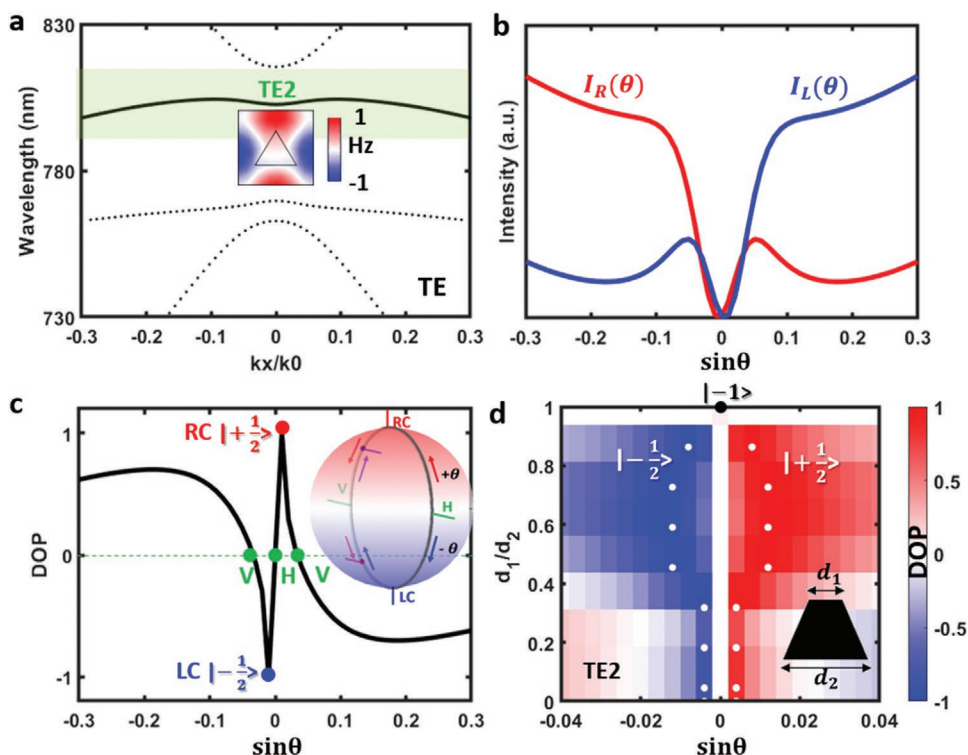


Figure 2. The virtual optical states of the metasurface. a) The VOS with TE polarized field in the metasurface and in-plane wavevectors along the x -axis. The optical band TE2 highlighted in green manifests as a quadrupole state at $k = 0$. The inset shows its field distribution within each unit cell on the x - y plane. b) Distribution of far-field electric field intensities with opposite handedness projected from TE2 as a function of radiation angle θ . c) DOP of the radiated field from TE2 versus radiation angle θ . The corresponding field vectors are mapped onto a Poincaré sphere, as a black vertical loop, to illustrate the full control of polarization. The field is linearly polarized at $\theta = 0$ (H) and $\sin\theta = \pm 0.035$ (V), purely circularly polarized at $\sin\theta = \pm 0.005$ (RC and LC), and strongly circularly polarized at large radiation angles with $DOP > \pm 60\%$. d) 2D colormap showing how the angular distribution of the calculated DOP for the TE2 VOS changes with the degree of symmetry in the metamolecule (here represented by the symmetry d_1/d_2 of a trapezoid). The white dots indicate the separation angle θ of the circularly polarized states with half-integer charges as a function of symmetry factor. Note that the radiative states are linearly polarized for $d_1/d_2 = 1$ (square metamolecule), when the in-plane inversion symmetry is restored (black dot).

a vertical loop across the two poles representing circular polarizations RC and LC , and the equator corresponding to linear polarizations H and V . The angular separation between circularly polarized states with half-integer charges can be modified by either adjusting the symmetry factor, d_1/d_2 , of the metamolecule (Figure 2d and Figure S3, Supporting Information), i.e., increasing/decreasing the in-plane inversion symmetry breaking, or by selecting different optical bands (Figure S3, Supporting Information). Figure 2d shows how the DOP associated with the TE2 band changes when the metamolecule evolves from a square to a triangular shape. The white dots in the figure track the angular position of the far-field projection of half-integer charges (i.e., fully circularly polarized radiative states) as a function of symmetry factor (by varying d_1 while keeping d_2 constant): without breaking in-plane inversion symmetry ($d_1/d_2 = 1$, square metamolecule) the radiative states are linearly polarized and the topological charge is -1 at $\sin\theta = 0$; when the symmetry factor decreases, the integer charge splits into two half-integer charges, leading to the separation of circularly polarized radiative states. Note that separation of circularly polarized radiative states on TE2 is not a linear function of the symmetry factor and reaches a maximum of $\sin\theta \approx 0.012$ at $d_1/d_2 \approx 0.6$.

The calculated far-field intensity distribution and polarization maps of TE2 in 2D momentum space are shown in Figure 3a, where each position in the map corresponds to a far-field radiation direction defined by the $\mathbf{k}_{\parallel} = (k_x, k_y)$. The polarizations across the radiated far-field vary from linear (H, V) to purely circular (RC, LC) with all intermediate polarization states, spanning the entire Poincaré sphere.^[11] Notably, circularly polarized radiation of different handedness is projected into opposite sectors of the hemisphere ($\pm k_x$) in the far field (Figure 3b,c). The calculated far-field DOP distribution of TE2 in the \mathbf{k}_{\parallel} space is shown in Figure 3d. DOP is of opposite sign in the two $\pm k_x$ hemispheres, reaching its maximum values of $DOP_{\text{sim}} = \pm 100\%$ at radiation angles close to the normal, and $DOP_{\text{sim}} > \mp 60\%$ moving away from the center of the momentum space. The simulation results indicate that the VOS of the metasurface is expected to project distinct far-field polarizations into well-separated directions.

The spatially varying far-field polarizations of TE2 can be imprinted onto the MAPbI₃ luminescence, routing the emitted light of designed polarizations into different, predetermined directions. The angular distribution of the photoluminescence (PL) emitted by the MAPbI₃ metasurface was measured by back-focal plane imaging in an optical microscope (setup

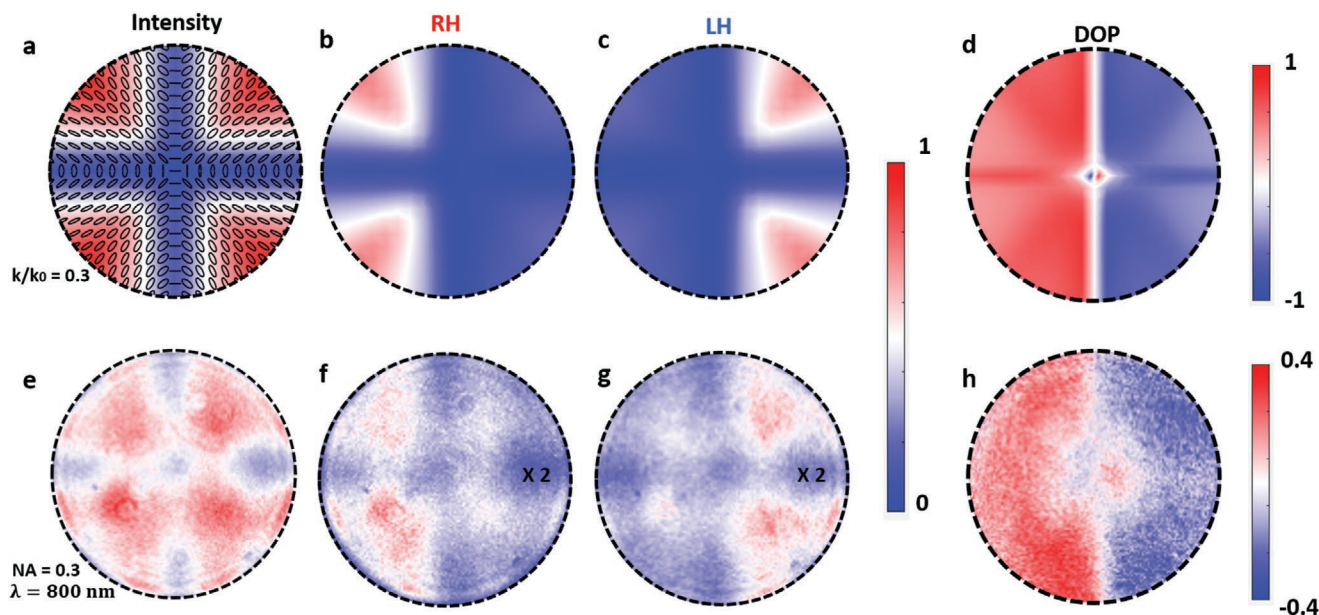


Figure 3. Optical Rashba effect of the light-emitting perovskite metasurface. a–d) The calculated far-field: a) total electric field intensity distribution and polarization map, b) right-handed polarized electric field intensity distribution, c) left-handed polarized electric field intensity distribution, and d) DOP distribution of TE2 in the momentum space (k_x, k_y). e–h) The measured total PL intensity distribution (e), right-handed polarized PL intensity distribution (f), left-handed polarized PL intensity distribution (g), and DOP of PL from the metasurface (h) in the back focal plane captured by a CCD with a 10 nm linewidth bandpass filter at 800 nm.

schematic in Figure S5, Supporting Information). The PL spectrum was filtered at $\lambda = 800$ nm to isolate the radiation coupled to TE2. The unpolarized emission was collected by an objective with numerical aperture (NA) of 0.3 and imaged by a CCD, using $\lambda/4$ waveplate and a linear polarizer to identify the chiral emission of opposite handedness. The measured intensity distributions of unpolarized, right and left circularly polarized PL and the DOP (Figure 3e–h) across a solid angle 175° (NA = 0.3) are in extremely good agreement with the numerical predictions (Figure 3a–d), which is the manifestation of optical Rashba effect. The experimental DOP reaches a remarkable value of $\text{DOP}_{\text{exp}} \approx \pm 40\%$. Note that, due to the bandwidth of the bandpass filter used in the measurements, the collected PL also includes off-resonance radiation channels and VOS with opposite chirality adjacent to TE2, thus the DOP_{exp} should only be considered as lower bound values.

The angular distribution and wavelength of the PL emission from the MAPbI₃ metasurface can be tuned by selecting different VOS or varying the geometric parameters of the metasurface. The principle is illustrated here by measuring the PL distribution at $\lambda = 810$ nm emitted by two metasurfaces with triangular metamolecules of side length $d = 220$ nm and $d = 250$ nm. A TE1 optical band can be isolated at 810 nm for both metasurfaces (Figure 4a), which manifests as a magnetic dipole state at $k = 0$, and an X-shaped DOP distribution in the two-dimensional momentum space (colormap in Figure 4b superimposed to the calculated far-field polarization). The spatial tunability of the circularly polarized PL at 810 nm is apparent in the experimental back focal plane intensity maps of the $d = 220$ nm (Figure 4c) and $d = 250$ nm (Figure 4d) metasurfaces, whose emission happens along a cone of 12° and 15° angle off the normal, respectively. The far-field distributions of the corresponding DOPs are underpinned

by the far-field polarization of TE1 and reach values as high as $\pm 60\%$, a sixfold increase over previous chiral perovskite demonstrations.^[18,19,33] In this case the separation of circularly polarized states in opposite half-hemispheres is reversed with respect to the emission underpinned by the TE2 band (Figure 3). Note that a separation of circularly polarized radiative states in the momentum space can also be observed for TM modes (Figure S4, Supporting Information).

Finally, not only the VOS spatially redistribute the chiral PL of the metasurface, they also induce a significant Purcell enhancement of the emission intensity. This is shown by the comparison of normalized PL emission maps and spatially integrated emission intensity of the unpatterned MAPbI₃ film and the metasurface (Figure 5). As expected, the PL from the unpatterned film around $\lambda = 800$ nm is isotropic (Figure 5a), while the metasurface shows spatial redistribution of the PL intensity with a maximum enhancement up to sixfold into specific directions (Figure 5b). The spectral dependence of the spatially integrated PL intensity of the unpatterned MAPbI₃ film and the metasurface are shown in Figure 5c, alongside the calculated enhancement, $\Gamma = I_{\text{MS}}/I_{\text{Film}}$. The enhancement reaches the maximum value of 4 at $\lambda = 800$ nm (the wavelength of the TE2 band), which is a manifestation of the Purcell effect. The PL enhancement at 810 and 780 nm is due to the Purcell effect from other VOS, i.e., TE1 and TM1 (Figure S4, Supporting Information).

3. Conclusion

We have demonstrated the optical Rashba effect in active MAPbI₃ perovskite metasurfaces with broken in-plane inversion

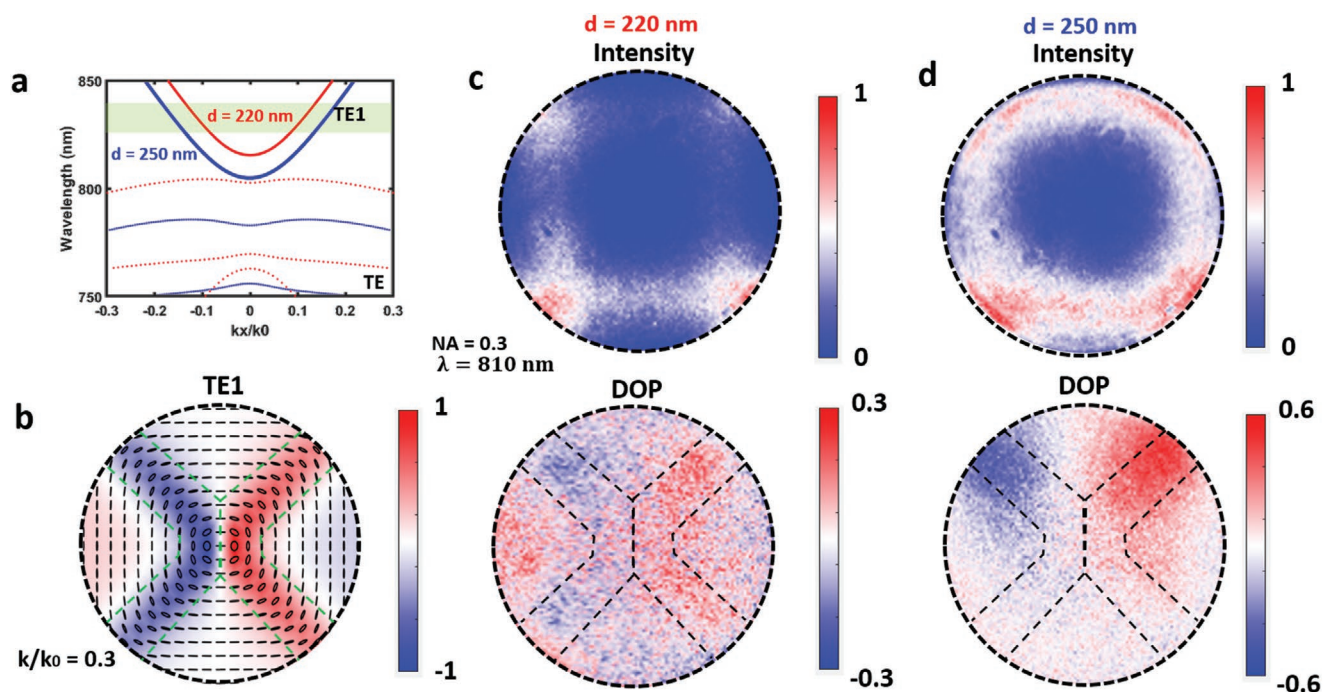


Figure 4. Control of chiral emission by metasurface design. a) Shift of the TE polarized VOS in the perovskite metasurfaces by varying the size of the triangular hole side length from $d = 220$ nm (red curves) to $d = 250$ nm (blue curves). b) Calculated far-field polarization map and DOP distribution of TE1 in the momentum space (k_x, k_y) at $\lambda = 810$ nm. c,d) Back focal plane maps of total PL intensity and DOP of triangular hole perovskite metasurfaces with $d = 220$ nm (c) and $d = 250$ nm (d) captured using a 10 nm bandpass filter at $\lambda = 810$ nm.

symmetry that allow generation, routing and enhancement of chiral photoluminescence. We experimentally achieved a DOP of 60% at room temperature and a sixfold enhancement of photoluminescence intensity due to the concurrence of Purcell effect and a far-field intensity redistribution. The implementation of the optical Rashba effect in a monolithic light-emitting materials platform represents a true analog of the electronic Rashba effect in condensed matter systems and may facilitate the development of planar light-emitting nano-devices with potential applications in holography, biosensing and encoding, polarization-division multiplexing and quantum optics.

4. Experimental Section

Film Preparation: Quartz substrates were cleaned by immersion in a mixture of 2 mL of Hellmanex II (Hellma Analytics) and 200 mL of deionized (DI) water at 353 K for 10 min, and subsequently rinsed with DI water and dried in nitrogen flow followed by oxygen plasma treatment. $\text{CH}_3\text{NH}_3\text{I}$ (Dyesol) and PbI_2 (99.99%, TCI) powders were added to anhydrous dimethylformamide (DMF, Sigma-Aldrich) and stirred for several hours at room temperature to form 1.2 M precursor solution (molar ratio 1:1) which was then filtered by a poly(vinylidene fluoride) (PVDF) syringe filter ($0.45 \mu\text{m}$) and heated on a hot plate at 373 K for 1 h. The hot solution was spin-coated onto quartz substrates at 4900 rpm for 30 s, with dripping of toluene after 5 s of spinning time. The prepared MAPbI_3 films were finally annealed at 373 K for 15 min. The

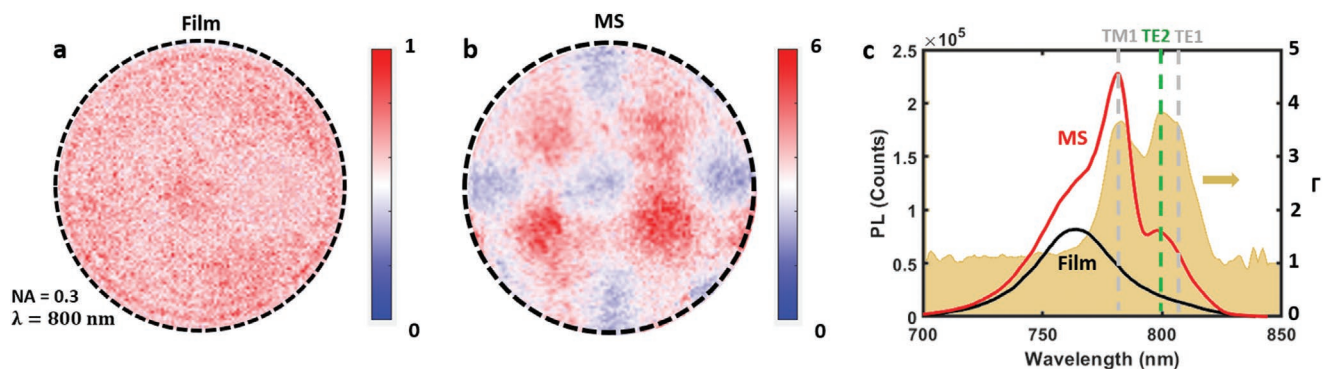


Figure 5. PL enhancement induced by the metasurface. a,b) The distribution of the PL intensity from a bare MAPbI_3 film (a) and the metasurface (b) captured by a 10 nm linewidth bandpass filter at 800 nm. The PL from the metasurface is normalized to that of the MAPbI_3 film. c) The overall PL spectra of the MAPbI_3 metasurface and a bare film along with the PL enhancement due to the metasurface.

precursor solution preparation and film fabrication steps were carried out in N₂-filled glovebox.

Mold Fabrication and Thermal Nanoimprint Lithography Process: A negative tone resist (hydrogen silsesquioxane, XR-1541-006) was spin-coated on a silicon substrate at a speed of 1500 rpm for 1 min. E-beam lithography was conducted to fabricate the triangle metasurface via ELS-7000 (Elionix Inc.) under an acceleration voltage of 100 kV and the dose of 7600 $\mu\text{C cm}^{-2}$. Inductively coupled plasma etching was employed as the following step to etch the Si substrate with a recipe of HBr (50 sccm) and O₂ (3 sccm) gases at 5 mTorr. Master molds were achieved after removing the HSQ mask in a buffered hydrofluoric acid. A nanoimprinter (Obducat NIL-60-SS-UV-Nano-imprinter) was used to transfer the metasurface from master mold to MAPbI₃ film at 30 bar and 90 °C, and the imprinting time was optimized as 30 min. The imprinted sample was cooled down to 30 °C and manually demolded from the master mold. Nanoimprint lithography was known to improve film uniformity and stability.^[34] The nanoimprinted metasurface was further protected by poly(dimethylsiloxane) (PDMS) encapsulation to increase its resistance to air and moisture.

Numerical Simulations: The optical bands of perovskite metasurfaces were calculated using the 3D finite-element method (COMSOL). One unit cell, consisting of a triangular hole at the center (with index of air), was simulated when embedded in a homogeneous background ($n = 1.5$). Periodic boundary conditions were adopted in both x and y directions and perfectly matched layers (PML) along the z -direction were constructed. The optical bands and the corresponding far-field vector distributions in the momentum space were calculated with an eigenfrequency solver by sweeping in-plane wavevectors.

Supporting Information

Supporting Information is available from the Wiley Online Library or from the author.

Acknowledgements

J.T. and G.A. contributed equally to this work. The authors acknowledge Jie Deng and Norman Soo Seng Ang for assistance with fabrication of the nanoimprint lithography mask. This research was supported by the A*STAR-AME programmatic fund on Nanoantenna Spatial Light Modulators for Next-Gen Display Technologies (grant A18A7b0058), and the Singapore Ministry of Education (Tier 3 grant MOE2016-T3-1-006).

Conflict of Interest

The authors declare no conflict of interest.

Data Availability Statement

The data that support the findings of this study are openly available in NTU research data repository DR-NTU (Data) at <https://doi.org/10.21979/N9/6ZW2EM>.

Keywords

bound states in the continuum, circularly polarized luminescence, directional emission, hybrid perovskite metasurfaces, monolithic integration, optical Rashba effect, Purcell enhancement

Received: November 12, 2021

Revised: December 13, 2021

Published online: February 14, 2022

- [1] G. Hu, X. Hong, K. Wang, J. Wu, H.-X. Xu, W. Zhao, W. Liu, S. Zhang, F. Garcia-Vidal, B. Wang, P. Lu, C.-W. Qiu, *Nat. Photonics* **2019**, *13*, 467.
- [2] P. P. Iyer, R. A. DeCrescent, Y. Mohtashami, G. Lheureux, N. A. Butakov, A. Alhassan, C. Weisbuch, S. Nakamura, S. P. DenBaars, J. A. Schuller, *Nat. Photonics* **2020**, *14*, 543.
- [3] K. Rong, B. Wang, A. Reuven, E. Maguid, B. Cohn, V. Kleiner, S. Katznelson, E. Koren, E. Hasman, *Nat. Nanotechnol.* **2020**, *15*, 927.
- [4] J. Wang, H. Li, Y. Ma, M. Zhao, W. Liu, B. Wang, S. Wu, X. Liu, L. Shi, T. Jiang, J. Zi, *Light: Sci. Appl.* **2020**, *9*, 148.
- [5] L. Sun, C.-Y. Wang, A. Krasnok, J. Choi, J. Shi, J. S. Gomez-Diaz, A. Zepeda, S. Gwo, C.-K. Shih, A. Alù, *Nat. Photonics* **2019**, *13*, 180.
- [6] C. W. Hsu, B. Zhen, A. D. Stone, J. D. Joannopoulos, M. Soljačić, *Nat. Rev. Mater.* **2016**, *1*, 16048.
- [7] B. Zhen, C. W. Hsu, L. Lu, A. D. Stone, M. Soljacic, *Phys. Rev. Lett.* **2014**, *113*, 257401.
- [8] M. Wu, S. T. Ha, S. Shendre, E. G. Durmusoglu, W. K. Koh, D. R. Abujetas, J. A. Sanchez-Gil, R. Paniagua-Dominguez, H. V. Demir, A. I. Kuznetsov, *Nano Lett.* **2020**, *20*, 6005.
- [9] C. Huang, C. Zhang, S. Xiao, Y. Wang, Y. Fan, Y. Liu, N. Zhang, G. Qu, H. Ji, J. Han, *Science* **2020**, *367*, 1018.
- [10] J. Tian, G. Adamo, H. Liu, M. Wu, M. Klein, J. Deng, N. S. S. Ang, R. Paniagua-Dominguez, H. Liu, A. I. Kuznetsov, arXiv: 2107.05239, 2021.
- [11] W. Liu, B. Wang, Y. Zhang, J. Wang, M. Zhao, F. Guan, X. Liu, L. Shi, J. Zi, *Phys. Rev. Lett.* **2019**, *123*, 116104.
- [12] T. Yoda, M. Notomi, *Phys. Rev. Lett.* **2020**, *125*, 053902.
- [13] V. S. Liberman, B. Y. Zel'dovich, *Phys. Rev. A* **1992**, *46*, 5199.
- [14] N. Shitrit, I. Yulevich, E. Maguid, D. Ozeri, D. Veksler, V. Kleiner, E. Hasman, *Science* **2013**, *340*, 724.
- [15] S. S. Kruk, M. Decker, I. Staude, S. Schlecht, M. Greppmaier, D. N. Neshev, Y. S. Kivshar, *ACS Photonics* **2014**, *1*, 1218.
- [16] Y. Plotnik, M. A. Bandres, S. Stützer, Y. Lumer, M. C. Rechtsman, A. Szameit, M. Segev, *Phys. Rev. B* **2016**, *94*.
- [17] G. Long, C. Jiang, R. Sabatini, Z. Yang, M. Wei, L. N. Quan, Q. Liang, A. Rasmita, M. Askerka, G. Walters, X. Gong, J. Xing, X. Wen, R. Quintero-Bermudez, H. Yuan, G. Xing, X. R. Wang, D. Song, O. Voznyy, M. Zhang, S. Hoogland, W. Gao, Q. Xiong, E. H. Sargent, *Nat. Photonics* **2018**, *12*, 528.
- [18] J. Ma, C. Fang, C. Chen, L. Jin, J. Wang, S. Wang, J. Tang, D. Li, *ACS Nano* **2019**, *13*, 3659.
- [19] Y. Z. Young-Hoon Kim, H. Lu, X. Pan, C. Xiao, E. Ashley Gauding, S. P. Harvey, J. J. Berry, Z. V. Vardeny, J. M. Luther, M. C. Beard, *Science* **2021**, *371*, 5.
- [20] G. Dresselhaus, *Phys. Rev.* **1955**, *100*, 580.
- [21] E. I. Rashba, V. I. Sheka, *Fiz. Tverd. Tela: Collect. Pap.* **1959**, *2*, 162; *New. J. Phys.* **2015**, *17*, 050202.
- [22] G. Bihlmayer, O. Rader, R. Winkler, *New J. Phys.* **2015**, *17*, 050202.
- [23] A. Manchon, H. C. Koo, J. Nitta, S. Frolov, R. Duine, *Nat. Mater.* **2015**, *14*, 871.
- [24] D. Niesner, M. Wilhelm, I. Levchuk, A. Osvet, S. Shrestha, M. Batentschuk, C. Brabec, T. Fauster, *Phys. Rev. Lett.* **2016**, *117*, 126401.
- [25] Y. Zhai, S. Baniya, C. Zhang, J. Li, P. Haney, C.-X. Sheng, E. Ehrenfreund, Z. V. Vardeny, *Sci. Adv.* **2017**, *3*, 1700704.
- [26] K. Frohna, T. Deshpande, J. Harter, W. Peng, B. A. Barker, J. B. Neaton, S. G. Louie, O. M. Bakr, D. Hsieh, M. Bernardi, *Nat. Commun.* **2018**, *9*, 1829.
- [27] M. T. Pham, E. Amerling, H. M. Luong, H. T. Pham, G. K. Larsen, L. Whittaker-Brooks, T. D. Nguyen, *Sci. Rep.* **2020**, *10*, 4964.
- [28] S. Makarov, A. Furasova, E. Tiguntseva, A. Hemmetter, A. Berestennikov, A. Pushkarev, A. Zakhidov, Y. Kivshar, *Adv. Opt. Mater.* **2019**, *7*, 1800784.
- [29] M. Abdi-Jalebi, Z. Andaji-Garmaroudi, S. Cacovich, C. Stavarakas, B. Philippe, J. M. Richter, M. Alsaari, E. P. Booker, E. M. Hutter,

- A. J. Pearson, S. Lilliu, T. J. Savenije, H. Rensmo, G. Divitini, C. Ducati, R. H. Friend, S. D. Stranks, *Nature* **2018**, 555, 497.
- [30] G. Xing, N. Mathews, S. S. Lim, N. Yantara, X. Liu, D. Sabba, M. Gratzel, S. Mhaisalkar, T. C. Sum, *Nat. Mater.* **2014**, 13, 476.
- [31] S. V. Makarov, V. Milichko, E. V. Ushakova, M. Omelyanovich, A. Cerdan Pasaran, R. Haroldson, B. Balachandran, H. Wang, W. Hu, Y. S. Kivshar, A. A. Zakhidov, *ACS Photonics* **2017**, 4, 728.
- [32] G. Adamo, H. N. Swaha Krishnamoorthy, D. Cortecchia, B. Chaudhary, V. Nalla, N. I. Zheludev, C. Soci, *Nano Lett.* **2020**, 20, 7906.
- [33] J. Wang, C. Fang, J. Ma, S. Wang, L. Jin, W. Li, D. Li, *ACS Nano* **2019**, 13, 9473.
- [34] Z. Li, J. Moon, A. Gharajeh, R. Haroldson, R. Hawkins, W. Hu, A. Zakhidov, Q. Gu, *ACS Nano* **2018**, 12, 10968.